WILEY | Hindawi

Research Article

Hybrid Controlled Multi-Input DC/DC Converter for Electric Vehicle Application

Mohan Bharathidasan [1], **Vairavasundaram Indragandhi** [1], **and Belqasem Aljafari** [2]

^{1}School of Electrical Engineering, Vellore Institute of Technology, Vellore 632014, India
^{2}Department of Electrical Engineering, Najran University, Najran 11001, Saudi Arabia

Correspondence should be addressed to Vairavasundaram Indragandhi; indragandhi.v@vit.ac.in

The use of energy sources for electric vehicle (EV) applications relies heavily on the power electronic interlinking and its successful control mechanism. A hybrid adaptive neuro-fuzzy inference system (ANFIS) proportional-integral (PI) based control strategy for a multi-input DC-DC converter is investigated in-depth for this purpose. At steady state, the proposed hybrid ANFIS PI controller uses the standard PI controller, and during the transient state, the ANFIS PI control strategy is used. Furthermore, the proposed control scheme aids in the tracing of a predetermined speed pattern in order to achieve total EV. A detailed simulation analysis of the proposed control strategy is carried out and its performace was compared with traditional controllers. The result indicated that the designed control strategy is reliable since it offers bidirectional power management, high gain with quick reaction, and low steady-state error. It enables rapid tracking and achieves improved dynamic response through increased flexibility and energy efficiency. The proposed scheme reduces component stress, as demonstrated by a reliability assessment using the MIL-HDBK-217F military handbook. At nominal power, the converter achieves 96.954% efficiency. An 80 W converter prototype was created and tested in the laboratory to monitor the real-time system's response time.

1. Introduction

Hybrid energy systems are one of the rapidly evolving technologies able to meet future energy demands. Operators and regulators are being asked to address the issue of connecting renewable energy sources to the grid [1]. Among the most important industries, the automobile sector is taking steps toward sustainability. It is a major source of air pollution; EVs are gaining famous all around the world, ushering in a new era of automotive sustainability. Initiatives in the field of renewable energy systems are also happening all over the world. Many different types of energy have been combined to create self-sufficient energy-producing systems [2, 3]. Solar energy [4, 5] is the most extensively used renewable energy source; however, they are unreliable. As a result, the use of energy storage systems in stand-alone applications such as fuel cell applications [6] is justified. In order to overcome the limits of typical step-up converters in

the use of higher voltage gain, the authors of [7–9] demonstrate a variety of high-gain DC-DC converters. Traditional DC-DC step-up converters face the issue of boosting voltage at large duty cycles, imposing excessive stress on the converter's power semiconductor components, diminishing overall efficiency, and restricting voltage gain [10–12]. The isolated multi-input converters and nonisolated multi-input converters are presented in [13–16]. The majority of the research suggests unidirectional multi-input converters based on the pulsing source cell concept, which cannot be used in energy storage systems or EVs. For the reverse flow of electricity in these applications, regenerative braking is required.

Numerous isolated multi-input and single-output DC-DC converters have been reported in the literature. Based on the coupling transformer, these converters can be divided broadly into isolated and nonisolated topologies. The performance of two inputs and one output isolated

DC-DC converters is presented in [17]. The literature presents a number of nonisolated multi-input and single-output DC-DC converters. For EV applications, a dual input, dual output DC-DC converter is described [18]. If there is only one input source available, this converter can deliver power independently from that source. It can also deliver power from two input sources simultaneously. A novel DC-DC converter is reported for EV applications using battery/ultracapacitor energy sources [19]. It has the ability to recharge input sources from the regenerative braking system, which increases the vehicle's efficiency and mileage by recovering energy during braking.

However, these converters lack the capability to simultaneously supply power from the battery and ultracapacitor to the vehicle load. The integration of renewable energy sources with EVs is proposed using a bridge-type multi-input DC-DC converter [20]. Similar to this, many of the converters have been proposed transmit power from the input sources to the load both concurrently and individually. However, it is not possible to charge one source from another using the same power converter. An interleaved soft-switched boost converter without any auxiliary switch is presented in [21]; by sending the energy held in the capacitor and resonant inductor to the output, the auxiliary resonant cell raises the voltage gain. An LC series single stage with switch capacitors is used to construct an easily adjustable voltage gain nonisolated DC-DC boost converter [22] utilizing the fewest possible components; the converter generates a DC-DC converter with a very high voltage gain. Auxiliary switches are used in [23] topology to ensure that there is no circulating current flowing across ports while allowing for bidirectional power flow at the battery port.

The auxiliary source must be charged from the primary source using a separate circuit. The system's overall cost is increased by this supplementary circuit. The basic structure of the multipowered hybrid electric vehicle (HEV) is shown in Figure 1. With a typical controller, bidirectional power flow with buck and boost operating modes was examined [24]. For the closed-loop current and voltage system regulation, traditional PI controllers are used, which results in a slow response [25, 26]. The authors of [27] implement an ANFIS controller to track the maximum power from a stand-alone photovoltaic (PV) system. The PV system is associated with the load via a DC-DC converter controlled by an ANFIS MPPT controller [28]. The two-quadrant inverter is described in [29] as ensuring the unidirectional power flow from its attached PV module to the output port through the high-frequency transformer. This action eliminates any possible circulating current among different ports. The authors of [30] propose a multi-input nonisolated interleaved DC-DC converter using coupled-inductor techniques. ANFIS was used to manage the voltage of a DC-DC converter [31] and to reduce error values [32]. Furthermore, a traditional controller did not enable reliable speed tracking of a predetermined speed profile when the converter is utilized for an EV application.

A fuzzy logic system with an online adaptive learning algorithm is presented [33] to improve the output voltage tracking performance of the DC-DC buck converters and to
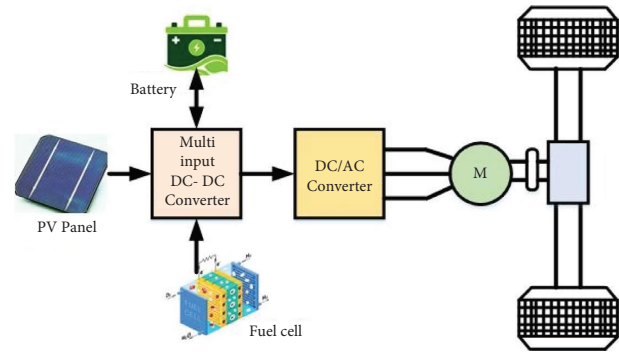

FIGURE 1: The multipowered HEV's basic structure.

offer smooth chattering in the switching control signal. This study proposes a hybrid ANFIS PI controller for this purpose, which has robust control. A standard PI controller in a steady state and an ANFIS PI controller in a transient state try to compensate for the hybrid ANFIS PI controller [34]. To highlight the system performance, the proposed controller performance is differentiated from that of a traditional controller. To restrict diode recovery and limit current, the resonant inductor is connected to the switched capacitor (SC).

The voltage gain of the converters is wide enough to meet the operation requirements of hybrid energy source EVs, especially [35] and can act as a power interface between the onboard dc bus and the low-voltage supercapacitor bank. On the other hand, these converters have a greater magnetic inrush current, a smaller static voltage gain, and higher output current ripples. The voltage gain is enhanced by adding a voltage lift capacitor and connected inductors to a high step-up DC-DC converter [36]. In addition, the converter uses an interleaved structure to reduce input ripple current. As a result, the system's overall switching and conduction losses have increased. Figure 2 shows a schematic diagram of an interleaved boost converter with a modified architecture. Inductive components are also utilized to transfer energy between sources and loads, resulting in higher dc gain than normal converters.

Furthermore, the suggested converters' interleaved design in both the input and output stages reduces not only minimum current ripples and the size of the input filter inductor but also conduction losses and efficiency. The grid is coupled via a novel multi-input DC-DC boost converter [37]. The battery may be charging and discharging during complete power management since the dc gain is increased. The coupled inductor's (CI) turn ratio is often raised in order to attain the appropriate voltage conversion ratio; input filters are required [38] and improve its efficiency and reliability. The CI is utilized to diminish the converter's inrush current while maintaining its DC properties. In CI converters, voltage-clamp circuits can provide good performance [39, 40].

To generate a larger boost converter, the [41, 42] converters use a voltage lift and CI. It integrates a soft-switching method and a CI using a parallel LC resonant tank circuit [43]. The CI [44], a nonisolated Quazi Z-source converter,
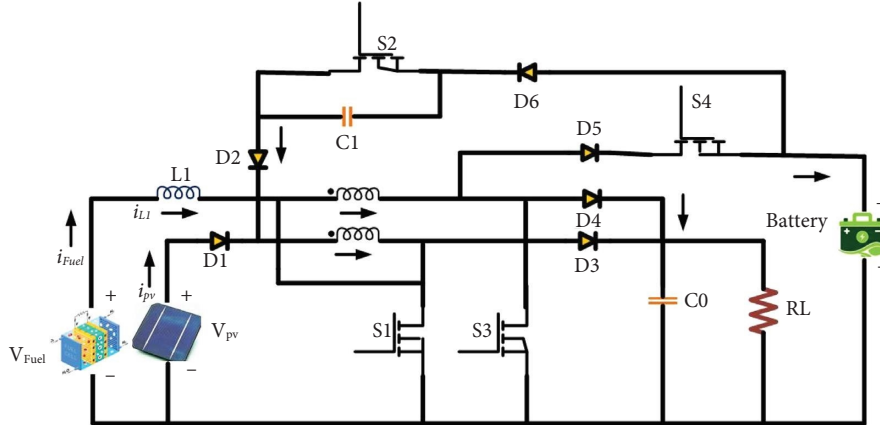
FIGURE 2: Interleaved multi-input converter with the coupled inductor.

reduces voltage stress between elements and components while enhancing voltage gain without lowering the duty cycle. A family of the switched boost DC-DC converter is presented in [45]. A hybrid Z-source boost DC-DC converter [46] satisfies the traditional benefits of Z-source networks with stronger voltage boost ability. Moreover, when the converter is used for EV application, a conventional controller does not provide robust speed tracking of a predefined speed profile. For this purpose, a hybrid ANFIS PI controller is proposed in this paper to have robust control. The performance of the proposed controller is compared with the conventional controller to spotlight the performance of the proposed scheme. The paper is organized into various sections as follows. The converter technique is proposed in Section 2, the design consideration of the proposed converter is shown in Section 3, the design of the proposed control scheme is shown in Section 4, the reliability analysis of the proposed converter is shown in Section 5, simulation results are shown in Section 6, experimental results are shown in Section 7, and conclusions are shown in Section 8.

2. Proposed Converter Topology

Figure 2 shows the schematic for a multi-input interleaved DC-DC converter beyond CI. It will increase the voltage gain, providing for high power density while reducing stress on power semiconductor components and reducing ripple current. It is specially matched for maximal-power applications since it allows for a reduction in input current ripple and conduction mode. V_{PV} and V_{FC} are autonomous sources whose output level is established upon characteristics. Input inductor (L_1) and magnetizing inductor (L_m) are in arrangement with PV and fuel cell (FC) modules. The R_L is equivalent to resistance to the load associated with the dc bus. Switch S1, S2, S3, and S4 are control switches. Diodes are utilized so as to set up the functions as described. Capacitor C1 is utilized to decrease stress, and output capacitor C0 is used as an output voltage filter.

By extending the steps of the interleaved converter, customized input current reduces the ripple. The inductor is ideally designed with a magnetizing, leakage, and two

winding of N_p and N_s. A current gets by the magnetizing inductance represent as ip and is. Exploiting from a high level of voltage gain, the used converter reaches the designated output level V_0 within the cycles. If the coupled inductor-based multi-input converter is working in continuous conduction mode (CCM) for an ideal converter, the ratio of steady-state output voltage to input voltage can be estimated.

$$M = \frac{V_0}{V_i} = \frac{(3+N)D}{1-D}, \tag{1}$$

where V_i is the input voltage, V_0 is the output voltage, D is the duty cycle, and N is the secondary inductor turn to primary inductor turn ratio. The duty cycle may be decreased with the same voltage gain by growing the turn ratio as (1). This technique uses a CI-based multi-input converter cell as a phase, with n of these phases attached in parallel to perform at the same duty ratio but with a ($2/n$) radian electrical angle phase shift. In an interleaved system, the number of cells, n, is primarily determined by the high voltage ratio and the load's higher power consumption. The designed converter has the benefit of employing only one resource in the event that the other power sources are unavailable. In a series configuration, each source can bypass the other to form a parallel connection through an individual diode which increases component counts. In the literature, most of the proposed topologies are inspired by basic DC-DC converter topology and have not been explored and synthesized completely, which leaves space for further improvement in the topological structure. This feature improves the proposed converter's safety and reliability. The followings are descriptions of many conceivable states.

2.1. FC OFF and PV ON. Due to the fuel cell's long start-up period, this condition usually occurs when the vehicle is first started or when the fuel cell gas runs out. PV can charge or discharge the battery while in this mode. This situation cannot last for long due to the fact that FC is the primary power source and ESS has a finite capacity. Switch S2 is disabled to allow the PV to run independently, and the PV's

power is transmitted to the output capacitor C0 instead of capacitor C1. The battery can be charged and discharged in the proposed topology by using PV and controlling switches S1, S3, and S4.

2.2. FC ON and PV OFF. As stated previously, FC is the primary power source for HEVs to meet their individual power needs because PV has lower energy and is more dependent on climate conditions than FC. As a result, capacitor C1 is paralleled by an additional diode (D5). When capacitor C1 is charged, diode D5 turns off. The capacitor C1 discharges until its voltage is zero when the FC is used independently. Diode D5 is activated when there is a negative voltage across capacitor C1, clamping the voltage of capacitor C1.

3. Design Consideration

3.1. Coupled-Inductor Design. The needed duty cycle and voltage gain evaluate the CI turn ratio. A low turn ratio is achieved when the duty cycle is maximum, which increases switch stress and necessarily requires the use of MOSFET with higher voltage levels and higher on-resistance. If the duty cycle is too low, a large turn ratio is required, resulting in maximum conduction loss and high leakage inductance. As a result, a solution must be discussed. The ZVS region's boundary is determined by CI leakage inductance. The leakage inductance in this configuration example is created to ensure ZVS functions from 40% to 100% load. Based on [47],

$$\left(4 - \frac{(n+2)^2}{(n+1)^2}\right) n^2 L_k i_0^2 > \left(C_{oss1} + C_{oss2}\right) V_{in}^2, \qquad (2)$$

where L_k indicates leakage inductor, i_0 indicates output current, and $Coss_1$ and $Coss_2$ are linear output capacitance.

Maintaining the continuous inductor current mode when providing a suitable current ripple in the magnetizing inductor is an excellent criterion for creating the L_m.

$$L_{m1} = L_{m2} = \frac{V_{in}D}{\Delta I_{Lm} f_s}, \qquad (3)$$

where D indicates duty cycle, f_s indicates switching frequency, and ΔI_{LM} indicates change in magnetizing inductor current.

The coupled inductor is created using the transformer design approach [47] after attaining zero dc bias. In reality, it can be complex to manage the leakage inductance correctly. An external inductor can be required to meet the ZVS criteria [48].

3.2. Input Inductor Design. The $L1$ is determined according to the appropriate ripples in the input current. The boost inductor can be measured by using a peak-to-peak ripple current r_L% of 5%.

$$L > \frac{V_{in}D}{r_L\%.I_L f_s} = \frac{V_{in}\left(V_0 - (n+2)V_{in}\right)}{r_L\%.I_L f_s V_0}, \qquad (4)$$

where a peak-to-peak current ripple r_L% of 5%, and I_L indicates inductor current

3.3. Capacitor Design. The capacitors' calculations are given by assuming a minimum voltage ripple (r_L%) of 2%.

$$C_1 = \frac{(N+1)I_0}{r_c\%V_{c1}f_s}. \qquad (5)$$

The following formula gives the value of the output capacitor,

$$C_{OUT\,(min)} = \frac{I_{OUT\,(max)} \times D}{f_s \times \Delta V_{OUT}}, \qquad (6)$$

$C_{OUT\,(min)}$ indicates minimum capacitor output, $I_{OUT\,(max)}$ indicates maximum current output, and ΔV_{OUT} indicates desirable ripple voltage output. The output capacitor equivalent series resistance (ESR) includes few additional ripples, as follows:

$$\Delta V_{OUT\,(ESR)} = ESR \times \left(\frac{I_{OUT(max)}}{1-D} + \frac{\Delta I_L}{2}\right), \qquad (7)$$

$\Delta V_{OUT\,(ESR)}$ indicates that ESR capacitors cause extra output voltage ripple.

The capacitors' RMS current stress is measured using

$$I_{Corms} = \frac{(1+D)I_0}{\sqrt{7D(1-D)}}. \qquad (8)$$

4. Proposed Control Scheme Design

Power flow management is a critical problem that requires a well-designed control scheme [49, 50]. A suitable control technique is proposed, which generates control signals (see Figure 3) to obtain the appropriate power from the sources simultaneously or separately with keeping a managed voltage. Before introducing measured signals to the controller, they are analyzed and sampled. The operating mode is selected in this system depending on the input condition and load demand, and control signals S2 and S4 are created correspondingly. The operational state is determined by the separate control of switching signals S2 and S4, which are dependent on the mode of operation. An approach for controlling the average current mode on the input stage with an outside voltage loop and an inner current control loop is utilized in the traditional PI control technique. The current through the inductor is regulated using this method by separately adjusting every current source for a particular load [51, 52]. In this study, a hybrid ANFIS PI controller replaces the traditional PI of voltage and current controllers. It allows for more flexibility in combining multiple characteristics sources to operate at their best levels, resulting in improved utilization and dynamic response [53].

The load side of an EV should have a motor, and energy sources such as FC, PV, or a battery supply may be employed. FC and PV with differential voltage magnitudes are used as energy sources in this study. As well to their differing dynamic and steady-state performance, each one
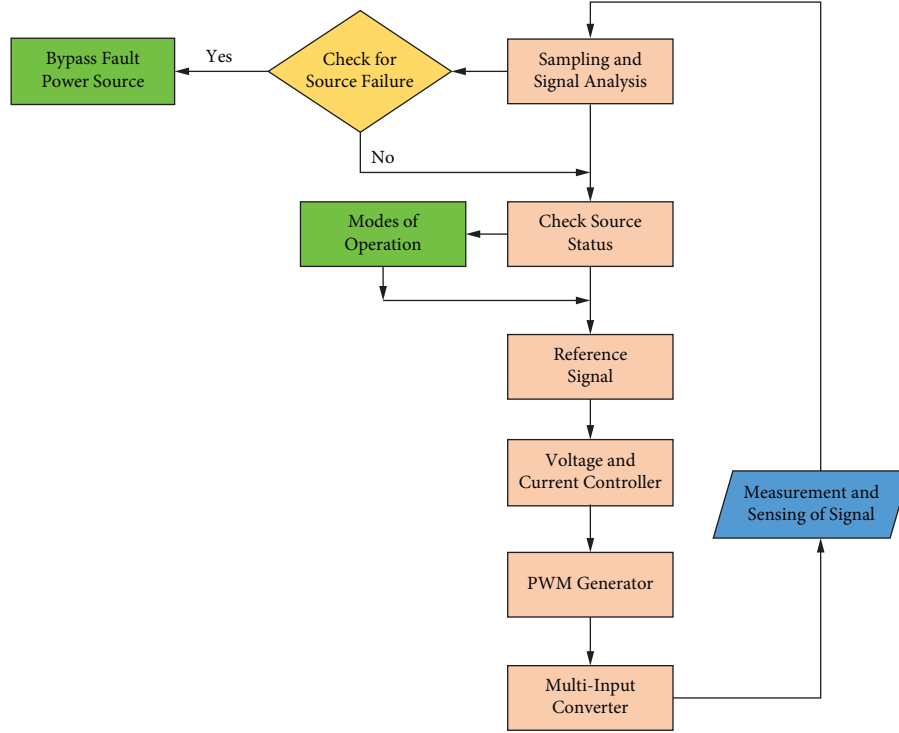
FIGURE 3: Multi-input converter control signal generation technique.

features diverse V-I characteristics and power handling capacity. As a load, a permanent magnet DC (PMDC) motor is used. As a result, the power management algorithm must be redesigned in this scenario, taking into account the motor's speed regulation during motoring and braking conditions, as illustrated in Figure 4. The use of a hybrid ANFIS PI controller allows for speed adjustment as well as inner loop two parallel current regulations. Since the converter output voltage is governed by the motor speed, the speed control achieves voltage control simultaneously.

The inner current controller regulates the current of the source by adjusting the duty cycle of the source's matching switch, which will provide a restricted power quantity. The proposed controller's aim is to integrate the greatest aspects of the PI and ANFIS controllers to deliver a greater response than any of them. This designed hybrid controller has a logical switching device that converts control actions from PI controller to ANFIS controller or vice versa, depending on the value of the speed deviation.

5. Reliability Analysis

The converters' component ratings are addressed in order to do the reliability evaluation. The reliability assessment is performed using the methods shown in Figure 5. Under standard operational and environmental conditions, reliability is the possibility that a system can execute as required. The device's performance is influenced not only by the fabrication technique and materials used but also by the work atmosphere. Engineers working in the field of power electronics must develop materials that can withstand a variety of conditions. By utilizing the military handbook,

the mean time to failure (MTTF) for the developed topology is evaluated for environmental factors. The failure rates of elements vary depending on their environment. Based on whether the element is utilized on the ground or in space, the failure rate varies. As a result, environmental factor πE will account for the impact of environmental conditions on failure rate. The failure rate of electronic elements [54] is measured according to MIL-HDBK-217F.

$$\lambda_{\text{component}} = \lambda_b \prod_{i=1}^{k} \pi_k, \tag{9}$$

where k represents the number of π variables that influence the element fail rate, and λ_b represents the element's fundamental failure rate.

The failure rate for every element in the converters is evaluated in this section, as well as the factors that influence it. The majority of element failure rates can be expressed in generic terms as

$$\lambda_p = \lambda_b . \pi_T . \pi_Q . \pi_E \frac{\text{Failures}}{10^6 h} . \tag{10}$$

Thermal, quality, and environmental stressors are represented by the parameters π_T, π_Q, and π_E, accordingly. The reliability of the resulting topologies is calculated using a bottom-up technique. Inductors' hot spots and semiconductor devices' junction temperatures also influence the temperature factor. The fail rate is affected by both temperature and application (π_A) and quality factor (π_Q). The failure rate is regulated by the quality of materials used in device fabrication. The environmental factor (π_E) is assumed to be 1, similar to most reliability analyses in the literature.
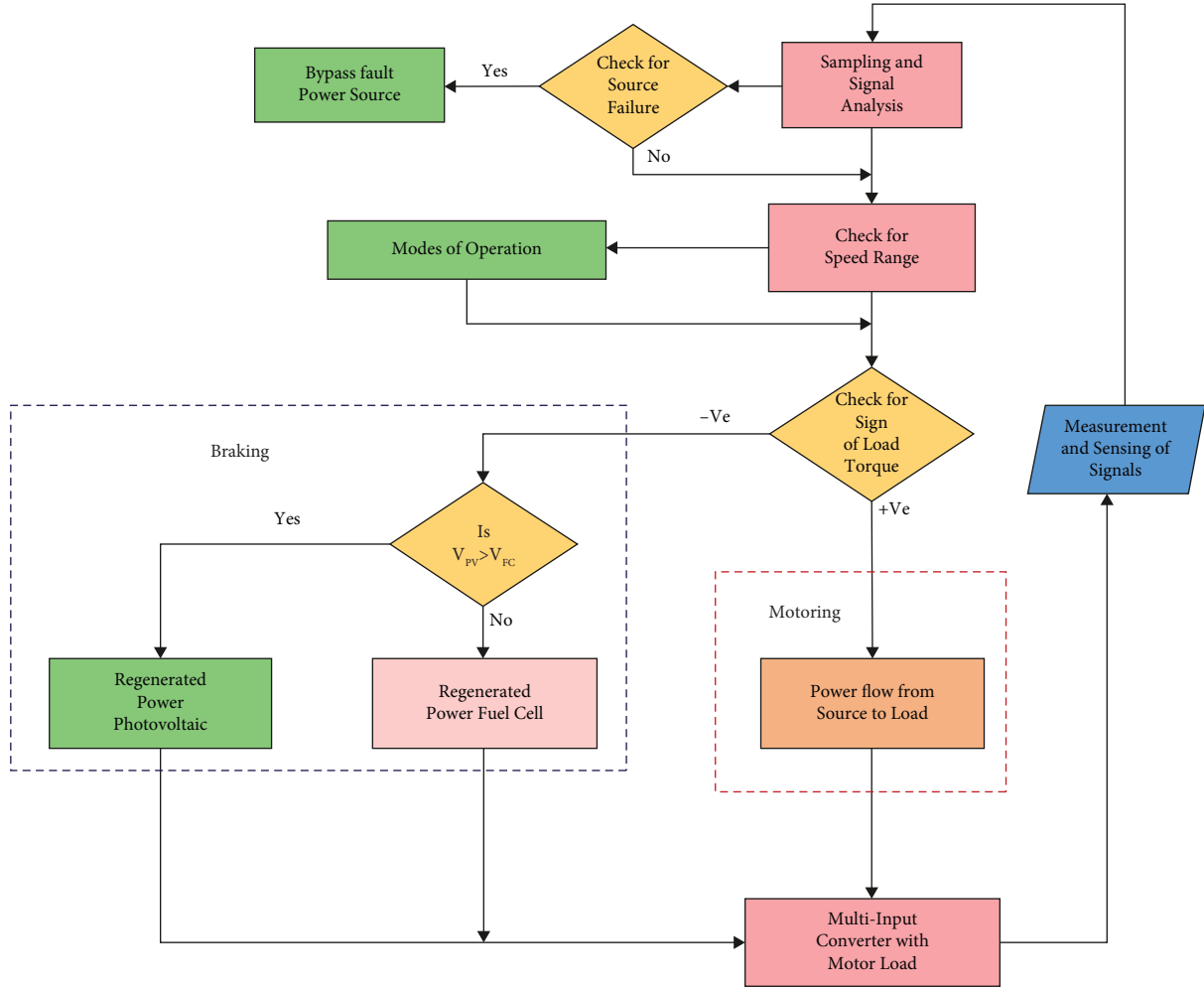
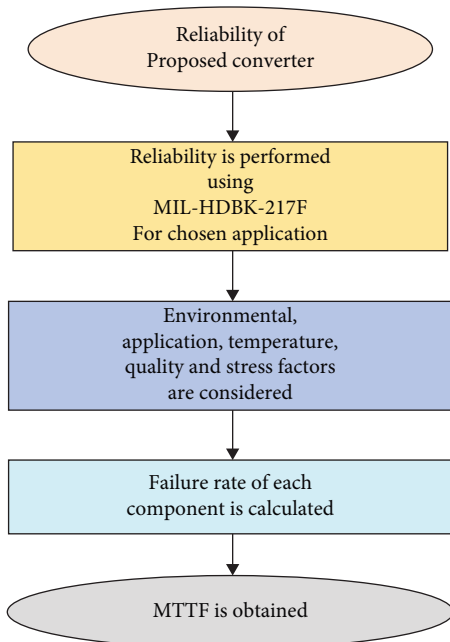FIGURE 4: A bidirectional power flow power management algorithm.

FIGURE 5: Procedures for conducting a reliability analysis.

However, according to the chosen applications, environmental concerns for all sections are considered in this work. The power loss impact in the converter components is used to determine the temperature effect on each part. As a result, the temperature is an important factor that regulates the component's failure rate. Temperature factor describes the effect of temperature on part failure rate; this is determined by the junction temperature of the component, T_j for hot-spot temperature or semiconductor devices, and T_{HS} for magnetic element.

5.1. Fail Rate of the Semiconductor Switch. The fail rate of switches is expressed as

$$\lambda_{SW} = \lambda_b \pi_T . \pi_A . \pi_Q . \pi_E \frac{\text{Failures}}{10^6 \, h}, \tag{11}$$

where π_A is the application factor. It specifies the element's power rating and its application utilization. In this scenario, that is a switching device rated at far less than 50 W. The class and grade of screening performed on the equipment determine the quality factor (π_Q). The values are stated in the handbook based on the qualification and power condition

tests. An environmental factor (π_E) can be used to adjust the influence of environmental pressures on the device in the real world. The environment in which the components are positioned on wheeled vehicles is represented by GM. The device's thermal stress is calculated by utilizing

$$\pi_T = \exp\left(-1925\left(\frac{1}{T_j + 273} - \frac{1}{298}\right)\right), \qquad (12)$$

where T_j is the temperature at the junction, and it is defined by

$$T_j = T_c + \theta_{jc}.P_{SW}. \qquad (13)$$

As shown in the previous equation, T_C is the case temperature; this is calculated using the handbook's defaulting case temperature setting. P_{sw} is the semiconductor switch's total power, and it is given in equation (14). θ_{JC} is the switch junction to case temperature from the semiconductor switch's datasheet. The power switch's thermal stress can be computed using the temperature at the junction. The thermal stress is lowered if the switch losses are lower.

Once the ZVS has been turned on, switching loss is disregarded. The switch's conduction loss is determined

$$P_S = I_{S1\_rms}^2 r_{on} + I_{S2\_rms}^2 r_{on} + I_{S3\_rms}^2 r_{on} + I_{S4\_rms}^2 r_{on}, \qquad (14)$$

where

$$I_{s1\_rms} = I_0 \sqrt{\frac{4(N+1)^2}{3D} + \frac{2(N+1)(N+2)}{1-D} + \frac{D(N+2)^2}{(1-D)^2}},$$

$$I_{s2\_rms} = I_{s3\_rms} = I_{s4\_rms} = I_0 \sqrt{\frac{4(N+1)^2 - 3N(N+2)}{3(1-D)}}. \qquad (15)$$

5.2. Fail Rate of Diodes.

The diodes fail rate is given as follows:

$$\lambda_D = \lambda_b.\pi_T.\pi_S.\pi_Q.\pi_E.\pi_c \frac{\text{Failures}}{10^6\,h}, \qquad (16)$$

where π_S is the electrical stress factor, and this is determined using the ratio of voltage stress. The voltage stress ratio is the proportion of applied voltage to rated voltage. Ratios of total voltage stress and electrical stress factors are determined for each topology, and π_S is selected from the handbook. π_C is the method of joining needed for creating contact on a printed circuit board (PCB) that determines the contacting configuration factor. The contact construction factor determines a consequence of physical interaction on the PCB with the diode (π_C). For metallurgically connected connections, this factor is unity. The temperature factor is stated as follows:

$$\pi_T = \exp\left(-3091\left(\frac{1}{T_j + 273} - \frac{1}{298}\right)\right), \qquad (17)$$

where T_j is the junction temperature, as defined by $T_j = T_C + \theta_{jc}.P_D$. and P_D stands for diode losses. The π_T factor is calculated simply as the MOSFET in the preceding section. The equation is used to calculate the power losses in diodes (18).

Conduction loss of a diode is calculated as follows:

$$P_{\text{diodes}} = \sum_{i=1}^{6} I_{D1}^2 R_{D1}. \qquad (18)$$

5.3. Fail Rate of Inductors.

The inductor type must be chosen first before the failure rate can be calculated. Inductors' failure rate is as follows:

$$\lambda_L = \lambda_b.\pi_Q.\pi_E.\pi_c \frac{\text{Failures}}{10^6\,h}, \qquad (19)$$

where a permanent inductor has been chosen, the construction factor π_C is one. The inductor's base fail rate is decided as 0.00035 $\exp(T_{HS} + 273/409)^{10}$ for insulation of class C. For applications working at temperatures above 125°C, class C insulation is recommended. T_{HS} stands for the temperature of the hot spot. The surface area that radiates and power loss experienced in the inductor are the two parameters to consider for the hot spot temperature study. This is provided by

$$T_{HS} = T_A + 1.1(\Delta T), \qquad (20)$$

where T_A is the inductive device ambient operating temperature (°C), ΔT is temperature rises on average above ambient $\Delta T = 125W_L/A$; and W_L is the loss of power in the scenario of a total radiating area (A). The following equation calculates the power loss caused by inductors.

$$P_L = I_L^2 r_L. \qquad (21)$$

Copper loss in a coupled inductor is calculated using

$$P_{CL\_copper} = I_{\text{pri\_rms}}^2 r_{\text{pri}} + I_{\text{sec\_rms}}^2 r_{\text{sec}}, \qquad (22)$$

where

$$I_{\text{pri\_rms}} = \frac{2nI_0}{\sqrt{3D(1-D)}},$$

$$I_{\text{sec\_rms}} = \frac{2I_0}{\sqrt{3D(1-D)}}, \qquad (23)$$

5.4. Failure Rate of Capacitors.

The capacitor failure rates are calculated using

$$\lambda_C = \lambda_b.\pi_Q.\pi_E.\pi_{CV} \frac{\text{Failures}}{10^6\,h}. \qquad (24)$$

Temperature and voltage loads on the elements have a significant influence on the fail rate at the base. π_{CV} is the capacitance factor determined by the capacitance value utilized in the converters, which is mostly determined by the capacitors' dielectric material. It is determined by 0.34 C0.18. The capacitor failure rate is determined in the same way as the other converter elements. The base failure rate of capacitors can be calculated using the following equation:

$$\lambda_b = 0.00254\left(\left(\frac{S}{0.5}\right)^3 + 1\right)\exp\left(5.09\left(\frac{T+273}{358}\right)^5\right), \quad (25)$$

where S is the working/rated voltage ratio, and T is the ambient temperature in °C. The following formula is used to calculate the capacitors' conduction loss:

$$P_{\text{capacitor}} = I_c^2 R_c. \quad (26)$$

The MTTF of the proposed scheme is calculated using the element failure rate [55, 56] from the aforementioned reliability study evaluation. The entire research is carried out while taking into account the environment in which EVs are used. The component failure rates in the proposed converter are as follows: $\lambda_{SW} = 6.654$ (Failures/106 h), $\lambda_D = 0.1493$ (Failures/106 h), $\lambda_L = 0.01396$ (Failures/106 h), $\lambda_C = 0.0298$ (Failures/106 h), MTTF (Khr) = 146.048. The suggested converter's and previous research's reliability evaluation curves are shown in Figure 6. The smaller the curve's slope, the greater the converter's reliability and MTTF.

6. Simulation Results

Initially, voltage control stabilization is carried out to evaluate the proposed controller's performance. The proposed converter simulation parameter is presented in Table 1. The input voltage is provided by connecting each input source in series. The voltage and current controllers are hybrid ANFIS PI controllers with parallel current gain settings that can be adjusted. When the error in speed is smaller than 5 rpm, the standard PI controller is activated; however, when the error is larger than 5 rpm, the ANFIS controller is activated. Figure 7 depicts the architecture of a hybrid ANFIS PI controller. It depends on the power quantity used from the sources over a specific length of time, either concurrently or individually, to satisfy a fluctuating load profile by working at all modes. The regenerated power must be given back to any of the energy sources during the braking state. During both driving and regenerative braking modes, the proposed controller provides a speed control function. Figure 8 shows the output current and voltage waveforms from the proposed simulation. There are no overshoots in the system's output voltage, which is well-managed at the desired level. There is an extremely little ripple in the system's output voltage. Figure 9 shows the voltage regulation in a defective situation.

The speed modulation for EVs is performed by a step-up mode of operation. Figure 10 illustrates the armature current through the motor and the speed modulation for a step interchange from 200 to 150 rad/s. Variation in the speed limit changes in the mode preference. For optimum EV

performance, speed control should be maintained throughout both motoring and braking. As shown in Figure 11, *a*, *b* illustrates the output voltage regulation and speed regulation comparison graphs for traditional PI, ANFIS, and hybrid ANFIS PI controllers. Tables 2 and 3 present the results of the performance investigation of several controllers. The table shows that the suggested hybrid ANFIS PI controller outperforms the traditional PI and ANFIS controllers. The flow of power from sources to the motor is used to adjust the speed for acceleration and motoring at a specific speed. The regenerated power is supplied back to the battery during deceleration. Therefore, charging of the battery takes place during braking operation of speed profile, which is depicted in Figure 12.

Figure 13 depicts an evaluation of the proposed converter's enhancing ability. Throughout all duty cycles, the proposed converter has the largest voltage.

The proposed converters are more reliable and similar to converters described in previous research, with lesser element voltage and current stress.

7. Experimental Verification

In this study, a prototype requirement of the circuit is designed and tested with an M62012P8060 programmable DC power supply to examine the converter performance. As stated previously, the proposed converter may be used for a variety of domestic and industrial applications in smart buildings, including HEV and DGs interface. To acquire experimental results, the DC power supply could be used instead of the current sources, disregarding the power sources' transient time. The inductor L1 is 10.67 mH, and the capacitors are 13.5 μF. Under these disturbances, the performance indicators evaluated are overshoot and undershoot in the output voltage, as well as the related settling times. The control strategy created utilizing the available CP1104 dSPACE board is found to be within allowed limits, confirming the control technique. After scaling, the output voltage of the proposed converter is sent to the CP1104's onboard ADC.

The hybrid ANFIS PI control technique devised correctly manipulates the duty cycle of the proposed converter based on the error between the planned output voltage and the actual output voltage during disturbances, and such PWM pulses provided by the CP1104 board are given to the gate of the SCT-3080-metal-oxide-semiconductorfield-effect transistor (MOSFET) by using appropriate drivers to maintain the desired output voltage. Figure 8 shows output voltages along with output current. Using 20 V for each input voltage that has been adequately raised to around 200 V, the efficiency of the converter is 96.954%. Initially, the proposed converter is tested with the lamp load. Figure 14 shows the proposed converter's acquisition inductor current and output voltage. A traction inverter is used to connect a BLDC motor to the converter's output as a load. The BLDC motor's rotation speed and direction are controlled by the throttle. Both sources provide the required power during acceleration mode, and step-up mode is used by the
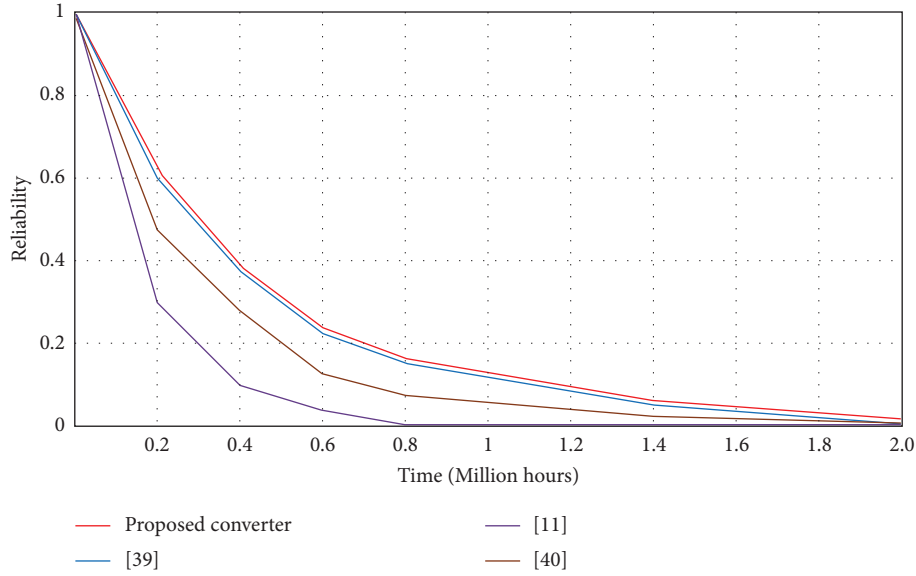
FIGURE 6: Reliability analysis.

TABLE 1: Proposed converter simulation parameters.

Symbol	Parameters	Range
V_{PV}, V_{FC}	Input voltages	20 V, 20 V
V_0	Output voltage	200 V
P_0	Output power	400 W
fs	Switching frequency	30 kHz
L_m	Magnetizing inductance	206 μH
L_k	Leakage inductance	3.8 μF
C_1, C_0	Capacitors	540 μF, 13.5 μF
R_L	Load resistance	100 Ω
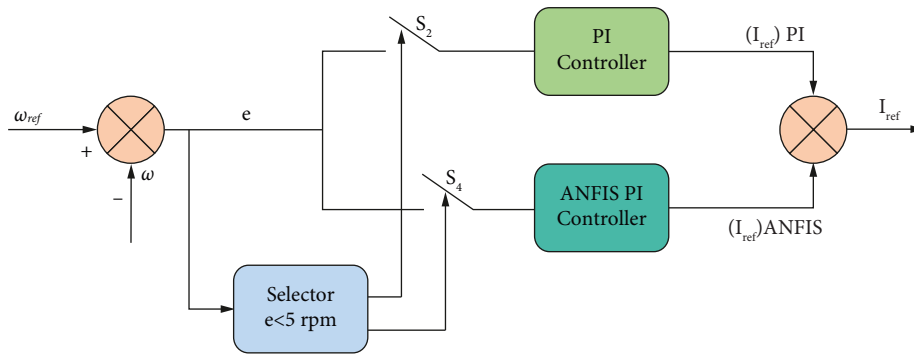
FIGURE 7: Structure of hybrid ANFIS PI controller.

proposed converter. The system's output voltage is ripple-free. This is also evident in the output power waveform, which has a very low ripple. Figure 15 depicts the experimental plot of the boost related to acceleration and constant speed operation. The voltage and current across the output capacitor are displayed in Figure 16. Figure 17 depicts the BLDC motor's hall signal and stator current under acceleration.
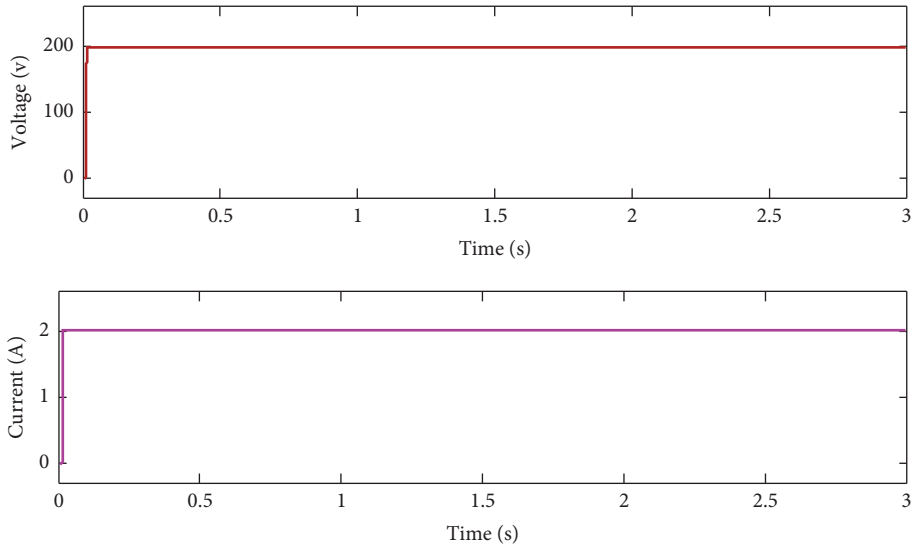
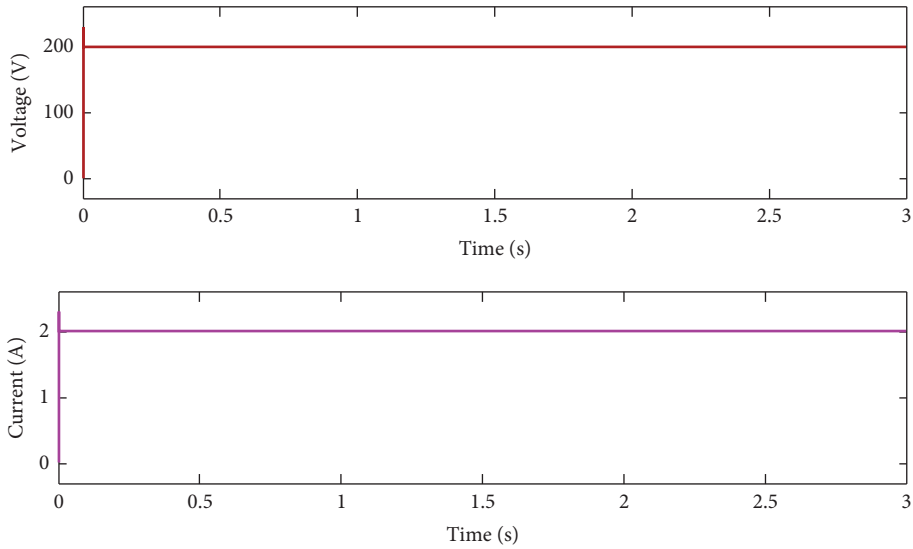Figure 8: Simulation results of output voltage and current.

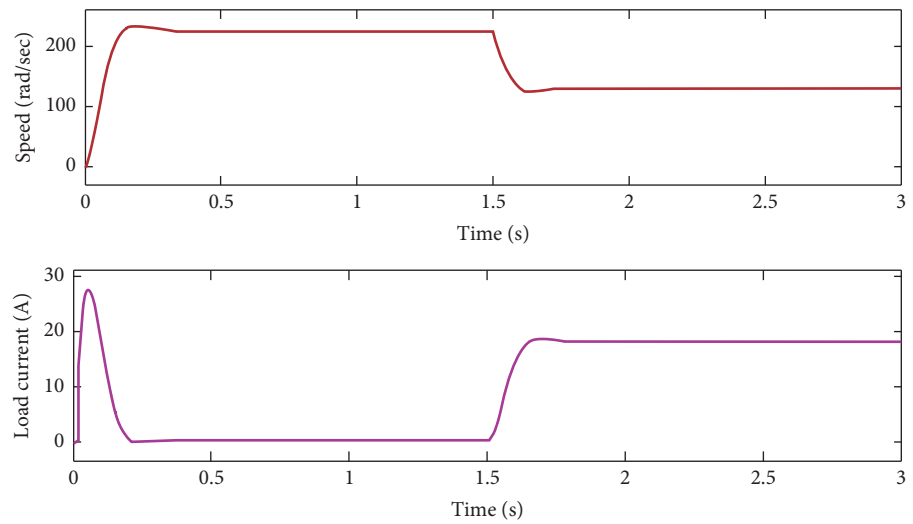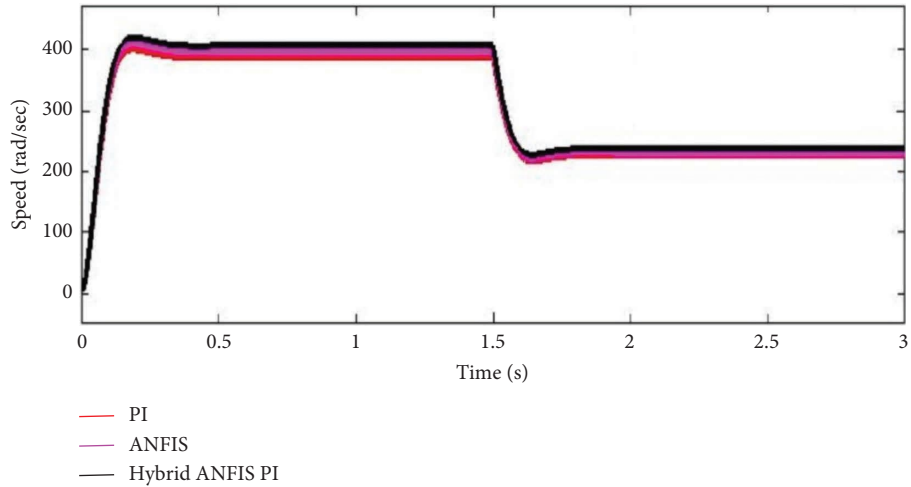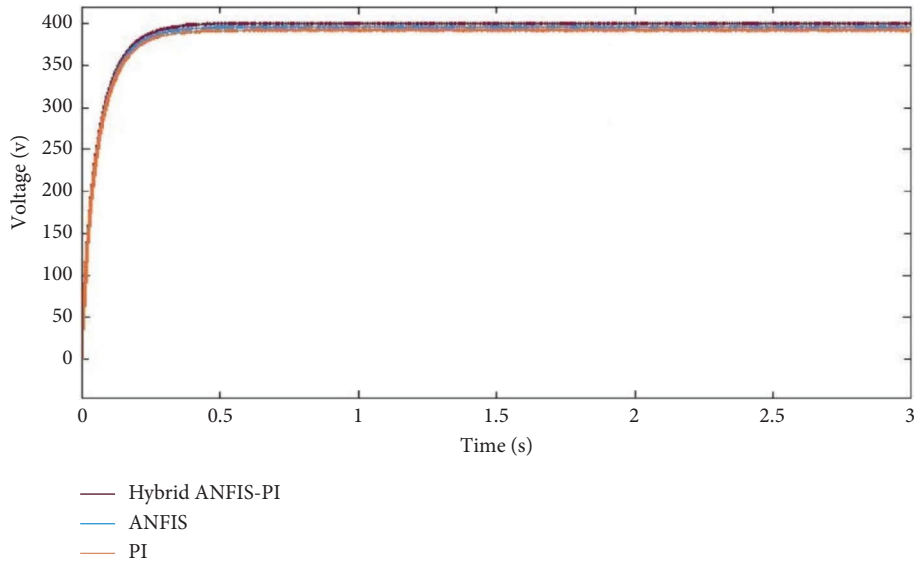Figure 9: Voltage regulation in a defective situation.

Figure 10: Step change speed modulation and armature current waveforms.

(a)

(b)

FIGURE 11: (a) For speed regulation, PI, ANFIS, and hybrid ANFIS PI controllers are compared. (b) For voltage regulation, PI, ANFIS, and hybrid ANFIS PI controllers are compared.

TABLE 2: Analyzing the performance of several voltage regulation controllers.

Rise time (s)	Peak time (s)	Settling time (s)	Steady-state error (V)	Controller
0.015	0.209	0.428	0.2215	PI
0.0147	0.207	0.432	0.2448	ANFIS
0.0144	0.202	0.398	0.1382	Hybrid ANFIS-PI

TABLE 3: Performance evaluation of several speed regulator controllers.

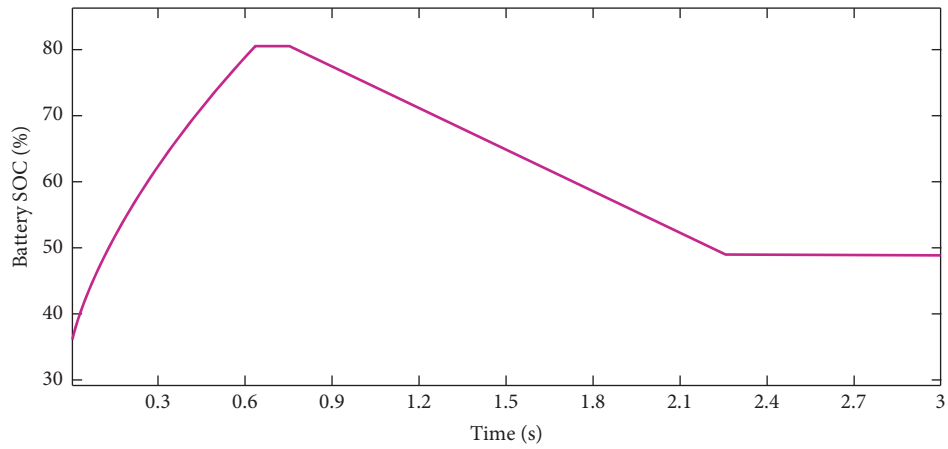| Rise time (s)	Peak time (s)	Settling time (s)	Steady-state error (rpm)	Controller
0.052	0.182	0.398	0.7261	PI
0.0471	0.164	0.387	0.6828	ANFIS
0.0421	0.127	0.302	0.6215	Hybrid ANFIS-PI

FIGURE 12: Charging and discharging of the battery during different operations of speed profile.
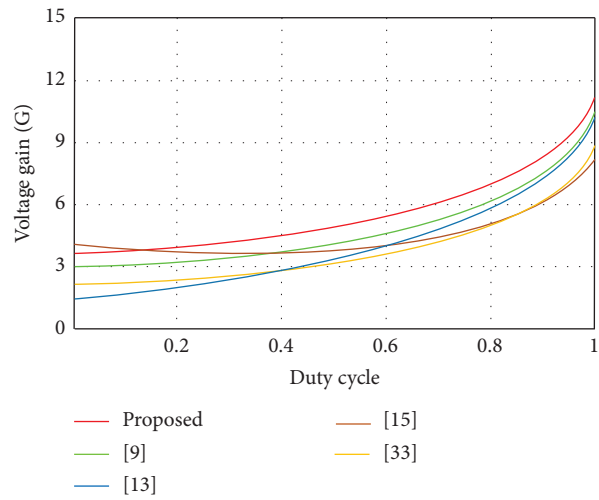

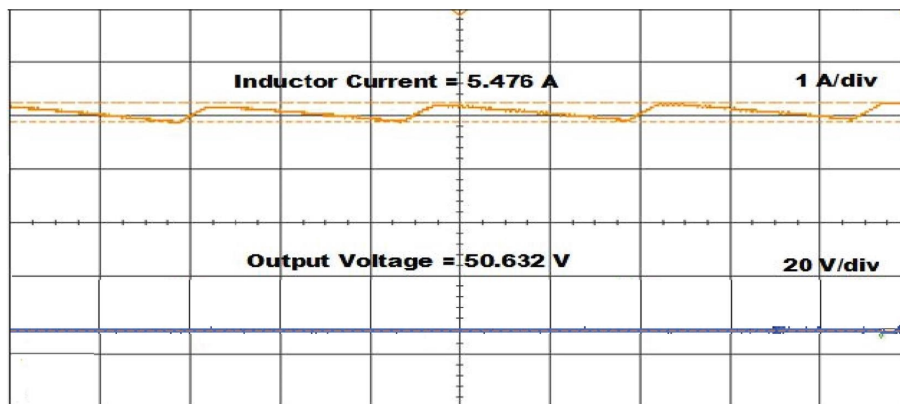FIGURE 13: Comparison curve of voltage gain vs. duty cycle.

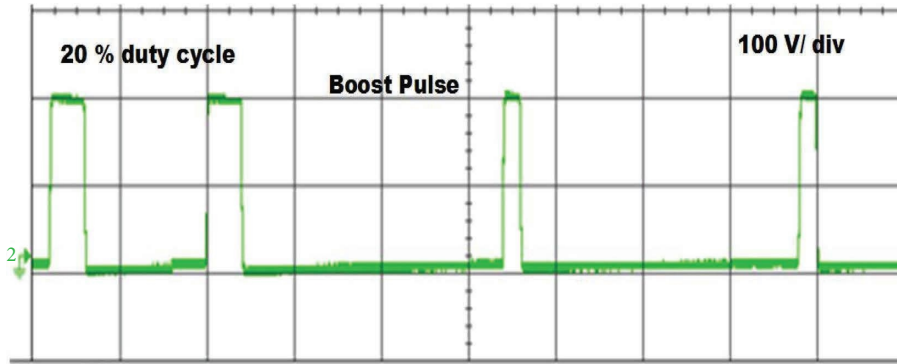FIGURE 14: The inductor current and output voltage proposed converter.

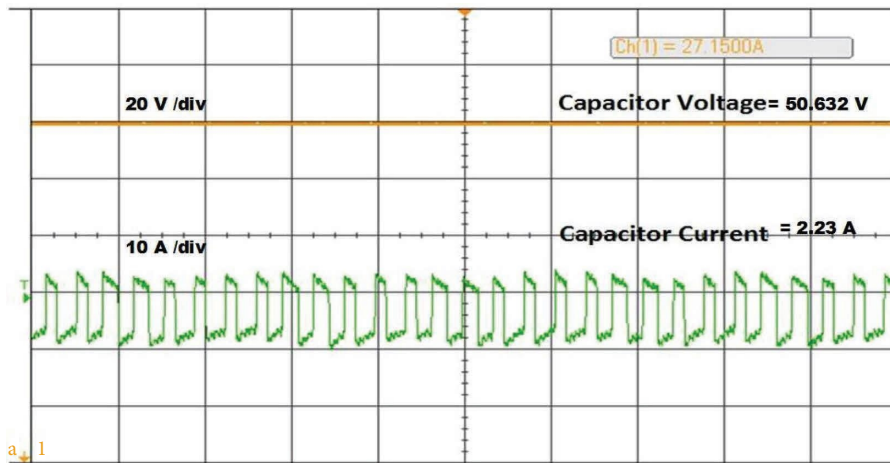FIGURE 15: Boost pulse waveform for acceleration and constant speed operation.

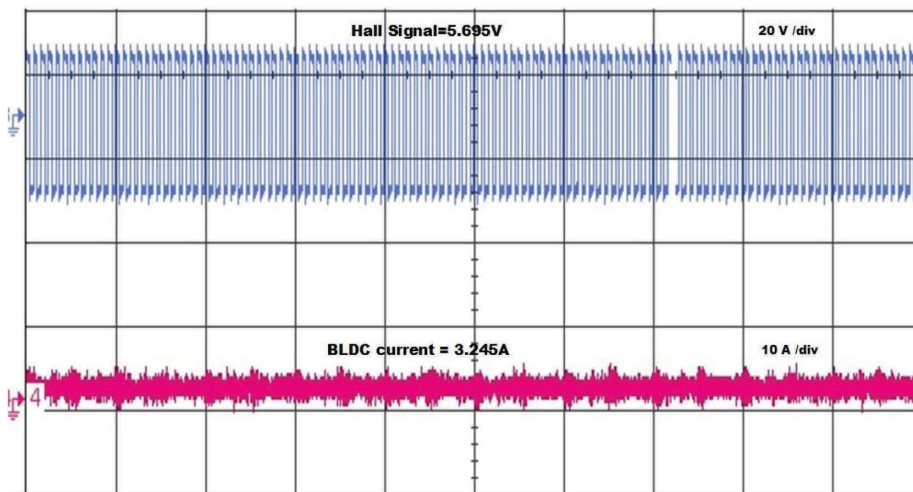
FIGURE 16: Output capacitor voltage and current.

FIGURE 17: Hall signal and stator current of BLDC motor during acceleration.

8. Conclusions

A hybrid ANFIS PI control technique for a proposed topology for EV application is implemented in this article. The designed power management control method, which makes use of a hybrid ANFIS PI controller, allows for bidirectional power management and reliable, quick tracking. In comparison to several converters described in the literature, the proposed converter has a high voltage ratio but a very small duty cycle. As a result, effective resource use and improved dynamic responses are offered. In comparison to other converters, the switches are subjected to too much less stress.

The recommended controller's performance is highlighted by a comprehensive simulation analysis, as well as performance evaluations with traditional controllers, which obstruct the better qualities of the PI and ANFIS controllers to generate greater response. The control rule is programmed in MATLAB/Simulink and runs in real time on the dSPACE (CP1104) board. The developed controller's robustness, tracking precision, and EV reliability were all highlighted in the experimental validation.

Data Availability

The data used to support the findings of this study are available from the corresponding author upon request.

Conflicts of Interest

The authors declare that there are no conflicts of interest regarding the publication of this paper.

References

[1] T. Kemabonta and M. Kabalan, "Integration of renewable energy resources from the perspective of the midcontinent independent system operator: a review," *The Electricity Journal*, vol. 31, no. 9, pp. 28–33, 2018.

[2] S. Reddi Khasim and C. Dhanamjayulu, "Selection parameters and synthesis of multi-input converters for electric vehicles: an overview," *Renewable and Sustainable Energy Reviews*, vol. 141, Article ID 110804, 2021.

[3] T. Mai, M. M. Hand, S. F. Baldwin et al., "Renewable electricity futures for the United States," *IEEE Transactions on Sustainable Energy*, vol. 5, no. 2, pp. 372–378, 2014.

[4] M. S. Pranav, K. Karunanithi, and M. Akhil, "Hybrid renewable energy sources (HRES)—a review," in *Proceedings of the 2017 International Conference on Intelligent Computing, Instrumentation and Control Technologies (ICICICT)*, pp. 162–165, IEEE, Kerala, India, July, 2017.

[5] S. R. Khasim, C. Dhanamjayulu, S. Padmanaban, J. B. Holm-Nielsen, and M. Mitolo, "A novel asymmetrical 21-level inverter for solar PV energy system with reduced switch count," *IEEE Access*, vol. 9, pp. 11761–11775, 2021.

[6] C. Dhanamjayulu, S. R. Khasim, S. Padmanaban, G. Arunkumar, J. B. Holm-Nielsen, and F. Blaabjerg, "Design and implementation of multilevel inverters for fuel cell energy conversion system," *IEEE Access*, vol. 8, pp. 183690–183707, 2020.

[7] A. Rajaei, R. Khazan, M. Mahmoudian, M. Mardaneh, and M. Gitizadeh, "A dual inductor high step-up DC/DC converter based on the Cockcroft–Walton multiplier," *IEEE Transactions on Power Electronics*, vol. 33, no. 11, pp. 9699–9709, 2018.

[8] S. Padmanaban, C. Dhanamjayulu, and B. Khan, "Artificial neural network and Newton Raphson (ANN-NR) algorithm based selective harmonic elimination in cascaded multilevel inverter for PV applications," *IEEE Access*, vol. 9, pp. 75058–75070, 2021.

[9] S. Sathyan, H. M. Suryawanshi, B. Singh, C. Chakraborty, V. Verma, and M. S. Ballal, "ZVS–ZCS high voltage gain integrated boost converter for DC microgrid," *IEEE Transactions on Industrial Electronics*, vol. 63, no. 11, pp. 6898–6908, 2016.

[10] S. Khosrogorji, M. Ahmadian, H. Torkaman, and S. Soori, "Multi-input DC/DC converters in connection with distributed generation units–A review," *Renewable and Sustainable Energy Reviews*, vol. 66, pp. 360–379, 2016.

[11] N. Zhang, D. Sutanto, and K. M. Muttaqi, "A review of topologies of three-port DC-DC converters for the integration of renewable energy and energy storage system," *Renewable and Sustainable Energy Reviews*, vol. 56, pp. 388–401, 2016.

[12] S. Saravanan and N. Ramesh Babu, "RBFN based MPPT algorithm for PV system with high step-up converter," *Energy Conversion and Management*, vol. 122, pp. 239–251, 2016.

[13] M. Forouzesh, Y. Shen, K. Yari, Y. P. Siwakoti, and F. Blaabjerg, "High-efficiency high step-up DC-DC converter with dual coupled inductors for grid-connected photovoltaic systems," *IEEE Transactions on Power Electronics*, vol. 33, no. 7, pp. 5967–5982, 2018.

[14] M. K. Nguyen, T. D. Duong, and Y. C. Lim, "Switched-capacitor-based dual-switch high-boost DC-DC converter," *IEEE Transactions on Power Electronics*, vol. 33, no. 5, pp. 4181–4189, 2018.

[15] M. L. Alghaythi, R. M. Connell, and N. E. Islam, "Design of a high step-up DC-DC power converter with voltage multiplier cells and reduced losses on semiconductors for photovoltaic systems," in *Proceedings of the 2019 IEEE Electric Ship Technologies Symposium (ESTS)*, pp. 214–218, IEEE, Washington, DC, USA, August, 2019.

[16] Y. Sato, M. Uno, and H. Nagata, "Non-isolated multiport converters based on integration of PWM converter and phase-shift-switched capacitor converter," *IEEE Transactions on Power Electronics*, vol. 35, no. 1, pp. 455–470, 2020.

[17] A. Affam, Y. M. Buswig, A. K. B. H. Othman, N. B. Julai, and O. Qays, "A review of multiple input DC-DC converter topologies linked with hybrid electric vehicles and renewable energy systems," *Renewable and Sustainable Energy Reviews*, vol. 135, Article ID 110186, 2021.

[18] S. Kumaravel, R. AchathuparambilNarayanankutty, V. S. Rao, and A. Sankar, "Dual input–dual output DC-DC converter for solar PV/battery/ultra-capacitor powered electric vehicle application," *IET Power Electronics*, vol. 12, no. 13, pp. 3351–3358, 2019.

[19] F. Naseri, E. Farjah, and T. Ghanbari, "An efficient regenerative braking system based on battery/supercapacitor for electric, hybrid, and plug-in hybrid electric vehicles with BLDC motor," *IEEE Transactions on Vehicular Technology*, vol. 66, no. 5, pp. 1–3738, 2016.

[20] S. Athikkal, G. G. Kumar, K. Sundaramoorthy, and A. Sankar, "Performance analysis of novel bridge type dual input DC-DC converters," *IEEE Access*, vol. 5, pp. 15340–15353, 2017.

[21] M. Rezvanyvardom, A. Mirzaei, M. Shabani et al., "Interleaved step-up soft-switching DC–DC Boost converter without auxiliary switches," *Energy Reports*, vol. 8, pp. 6499–6511, 2022.

[22] H. Khalid, S. Mekhilef, M. B. Mubin et al., "Analysis and design of series-LC-switch capacitor multistage high gain

DC-DC boost converter for electric vehicle applications," *Sustainability*, vol. 14, no. 8, p. 4495, 2022.

[23] M. I. Marei, B. N. Alajmi, I. Abdelsalam, and N. A. Ahmed, "An integrated topology of three-port DC-DC converter for PV-battery power systems," *IEEE Open Journal of the Industrial Electronics Society*, vol. 3, pp. 409–419, 2022.

[24] H. Jigang, W. Jie, and F. Hui, "An anti-windup self-tuning fuzzy PID controller for speed control of brushless DC motor," *Automatika*, vol. 58, no. 3, pp. 321–335, 2017.

[25] R. Kandiban and R. Arulmozhiyal, "Speed control of BLDC motor using adaptive fuzzy PID controller," *Procedia Engineering*, vol. 38, pp. 306–313, 2012.

[26] A. Sabir and M. Kassas, "A novel and simple hybrid fuzzy/PI controller for brushless DC motor drives," *Automatika*, vol. 56, no. 4, pp. 424–435, 2015.

[27] A. A. Aldair, A. A. Obed, and A. F. Halihal, "Design and implementation of ANFIS-reference model controller based MPPT using FPGA for photovoltaic system," *Renewable and Sustainable Energy Reviews*, vol. 82, pp. 2202–2217, 2018.

[28] M. A. Sarhan, M. Ding, X. Chen, Y. Ou, and M. Wu, "ANFIS control for photovoltaic systems with DC-DC converters," in *Proceedings of the 2017 International Conference on Automation, Control and Robots*, pp. 9–14, Wuhan, China, December, 2017.

[29] B. N. Alajmi, M. I. Marei, and I. Abdelsalam, "A multiport DC–DC converter based on two-quadrant inverter topology for PV systems," *IEEE Transactions on Power Electronics*, vol. 36, no. 1, pp. 522–532, 2021.

[30] M. Bharathidasan, V. Indragandhi, R. Kuppusamy, Y. Teekaraman, S. Urooj, and N. Alwadi, "Intelligent fuzzy based high gain non-isolated converter for DC micro-grids," *Computers, Materials and Continua*, vol. 71, no. 2, pp. 4069–4084, 2022.

[31] I. H. Alsakini, M. D. Almawlawe, and I. A. Dahham, "Controlling switched DC-DC converter using ANFIS in comparison with PID controller IOP conference series: materials science and engineering," *IOP Conference Series: Materials Science and Engineering*, vol. 870, no. 1, Article ID 012130, 2020.

[32] D. Buvana and R. Jayashree, "ANFIS controller-based cascaded non-isolated bidirectional DC–DC converter," *Journal of Circuits, Systems, and Computers*, vol. 28, no. 1, Article ID 1950001, 2019.

[33] B. Babes, S. Mekhilef, A. Boutaghane, and L. Rahmani, "Fuzzy approximation-based fractional-order nonsingular terminal sliding mode controller for DC–DC buck converters," *IEEE Transactions on Power Electronics*, vol. 37, no. 3, pp. 2749–2760, 2022.

[34] A. Ramya, A. Imthiaz, and M. Balaji, "Hybrid self-tuned fuzzy PID controller for speed control of brushless DC motor," *Automatika*, vol. 57, no. 3, pp. 672–679, 2016.

[35] Y. Zhang, Q. Liu, Y. Gao, J. Li, and M. Sumner, "Hybrid switched-capacitor/switched-quasi-Z-source bidirectional DC–DC converter with a wide voltage gain range for hybrid energy sources EVs," *IEEE Transactions on Industrial Electronics*, vol. 66, no. 4, pp. 2680–2690, 2019.

[36] A. Mirzaei, M. Rezvanyvardom, and S. Mekhilef, "High step-up interleaved zero-voltage transition DC–DC converter with coupled inductors," *IET Power Electronics*, vol. 13, no. 19, pp. 4518–4531, 2020.

[37] R. R. Ahrabi, H. Ardi, M. Elmi, and A. Ajami, "A novel step-up multiinput DC–DC converter for hybrid electric vehicles application," *IEEE Transactions on Power Electronics*, vol. 32, no. 5, pp. 3549–3561, 2017.

[38] S. Dwari and L. Parsa, "An efficient high-step-up interleaved DC–DC converter with a common active clamp," *IEEE Transactions on Power Electronics*, vol. 26, no. 1, pp. 66–78, 2011.

[39] M. Premkumar, C. Kumar, and R. Sowmya, "Analysis and implementation of high-performance DC-DC step-up converter for multilevel boost structure," *Frontiers in Energy Research*, vol. 7, p. 149, 2019.

[40] Y. P. Siwakoti and F. Blaabjerg, "Single switch non-isolated ultra-step-up DC–DC converter with an integrated coupled inductor for high boost applications," *IEEE Transactions On Power Electronics*, vol. 32, no. 11, pp. 8544–8558, 2017.

[41] V. J. Samuel, G. Keerthi, and P. Mahalingam, "Coupled inductor-based DC–DC converter with high voltage conversion ratio and smooth input current," *IET Power Electronics*, vol. 13, no. 4, pp. 733–743, 2020.

[42] A. Kumar and P. Sensarma, "Ripple-free input current high voltage gain DC–DC converters with coupled inductors," *IEEE Transactions on Power Electronics*, vol. 34, no. 4, pp. 3418–3428, 2019.

[43] W. Hassan, D. D. C. Lu, and W. Xiao, "Analysis and experimental verification of a single-switch high-voltage gain ZCS DC–DC converter," *IET Power Electronics*, vol. 12, no. 8, pp. 2146–2153, 2019.

[44] A. Samadian, S. H. Hosseini, M. Sabahi, and M. Maalandish, "A new coupled inductor non-isolated high step-up quasi Z-source DC–DC converter," *IEEE Transactions on Industrial Electronics*, vol. 67, no. 7, pp. 5389–5397, 2020.

[45] X. Zhu, B. Zhang, Z. Li, H. Li, and L. Ran, "Extended switched-boost DC-DC converters adopting switched-capacitor/switched-inductor cells for high step-up conversion," *IEEE Journal of Emerging and Selected Topics in Power Electronics*, vol. 5, no. 3, pp. 1020–1030, 2017.

[46] H. Shen, B. Zhang, and D. Qiu, "Hybrid Z-source boost DC–DC converters," *IEEE Transactions on Industrial Electronics*, vol. 64, no. 1, pp. 310–319, 2017.

[47] Transformer Design with Magnetics Ferrite Cores Magnetics Inc, "Transformer Design with Magnetics Ferrite Cores, Magnetics, Inc," 2020, https://www.mag-inc.com/Design/Design-Guide/Transformer-Design-with-Magnetics-Ferrite-Cores.

[48] Phase-Shifted Full-Bridge, "Zero-voltage transition design considerations, application report," Texas instruments, boulevard Dallas, TX, USA, 2011, https://www.ti,com/lit/an/slua107a.pdf.

[49] Q. Li, W. Chen, Y. Li, S. Liu, and J. Huang, "Energy management strategy for fuel cell/battery/ultracapacitor hybrid vehicle based on fuzzy logic," *International Journal of Electrical Power and Energy Systems*, vol. 43, no. 1, pp. 514–525, 2012.

[50] W. Jiang and B. Fahimi, "Active current sharing and source management in fuel cell–battery hybrid power system," *IEEE Transactions on Industrial Electronics*, vol. 57, no. 2, pp. 752–761, 2009.

[51] L. Kumar and S. Jain, "A novel multiple input DC-DC converter for electric vehicular applications," in *Proceedings of the 2012 IEEE Transportation Electrification Conference and Expo (ITEC)*, pp. 1–6, IEEE, Dearborn, MI, USA, June, 2012.

[52] L. Kumar and S. Jain, "A multiple source DC/DC converter topology," *International Journal of Electrical Power and Energy Systems*, vol. 51, pp. 278–291, 2013.

[53] N. Tiwary, A. Rathinam, and S. Ajitha, "Design of Hybrid Fuzzy-PI controller for speed control of Brushless DC motor," in *Proceedings of theInternational Conference on Electronics,*

Communication and Instrumentation (ICECI), pp. 1–4, IEEE, Kolkata, India, January, 2014.

[54] Us Department of Defense, "Reliability prediction of electronic equipment," *In This Is Military Handbook For Reliability; MIL-HDBK-217*, Relex Software Corp, Greenburg, PA, USA, 1990.

[55] A. Khosroshahi, M. Abapour, and M. Sabahi, "Reliability evaluation of conventional and interleaved DC–DC boost converters," *IEEE Transactions on Power Electronics*, vol. 30, no. 10, pp. 5821–5828, 2015.

[56] M. Bharathidasan and V. Indragandhi, "Design and implementations of high step-up non isolated DC-DC converters for electric vehicles application," *International Journal of Circuit Theory and Applications*, vol. 50, 2022.